FULLY TURBULENT FLOW IN A PHYSIOLOGICALLY REALISTIC HUMAN AIRWAY BIFURCATION

Fotos S. Stylianou and Stavros C. Kassinos
Computational Sciences Laboratory (UCY-CompSci)
Department of Mechanical and Manufacturing Engineering
University of Cyprus, University Avenue 1, 2109 Nicosia, Cyprus
stylianou.fotos@ucy.ac.cy, kassinos@ucy.ac.cy

ABSTRACT

Recent computational studies have shown that the airflow in the upper human airways is turbulent during much of the respiratory cycle. A feature of respiratory airflow that poses a challenge to computations based on Reynolds-Averaged Navier-Stokes (RANS) closures is the laminar-turbulent-laminar transition as the flow moves from the mouth through the glottis and down to the lower conducting airways. Turbulence and unsteadiness are expected at least through the first few bifurcations of the airways. In the case of inhaled medicines, and depending on the size of the particles in the formulation, airway bifurcations are areas of preferential deposition. In this study we perform for the first time, Large Eddy Simulations (LES) and Direct Numerical Simulations (DNS) of fully developed turbulent flow through a single human airway bifurcation, emulating steady prolonged inspiration and expiration conditions. We also perform RANS simulations via the $\overline{v^2} - f$ closure model and compare with our DNS and LES results. We examine the mean flow characteristics and the turbulent vortical structures as well as their effect on the deposition of particles of different sizes.

INTRODUCTION

Predicting regional deposition patterns of inhaled aerosols is important for the design and optimization of pharmaceutical formulation-device products and for understanding the health effects of inhaled pollutants. The geometry of the airways greatly influences the local airflow structures, which in turn affect aerosol deposition. Geometrical variabilities in the respiratory tracts of patients complicate the efforts to understand patterns of regional deposition and point towards the need for patient-specific airflow analysis. In this regard, computer simulations can be used to predict regional deposition, thus helping in the development of targeted inhalation therapies that are customized, if not to individuals, at least to classes of patients. Such computations need to be based on realistic airway geometries, often obtained from patient CT-scans. They must also be able to handle reliably the unsteadiness and laminar-turbulent-laminar transition as one moves from the upper to the lower conducting airways. Furthermore, they need to be affordable for use in routine medical evaluations of patients. DNS are computationally too demanding for routine use, while LES is now becoming barely affordable. Thus, for routine computations the emphasis remains on the use of simplified

modeling approaches, such as RANS closures. Nevertheless, DNS and LES can be used to elucidate the regional flow characteristics in the conducting airways, thus helping to ensure that RANS computations are properly designed and tuned to capture the most important flow features. The upper airways are composed of building blocks that can be represented by idealized geometries in benchmark studies, e.g. straight and bend pipes, tubular constrictions and expansions, and single bifurcations. For most of the aforementioned building blocks, RANS models can be validated, and if necessary tuned, using turbulent benchmark data in the scientific literature. The single bifurcation geometry is an exception. To the best of our knowledge, turbulent flow through a bifurcation was never reported in the scientific literature. The aim of the present study is to use DNS and LES to characterize in detail the flow structures and particle deposition patterns in a realistic representation of a human airway bifurcation.
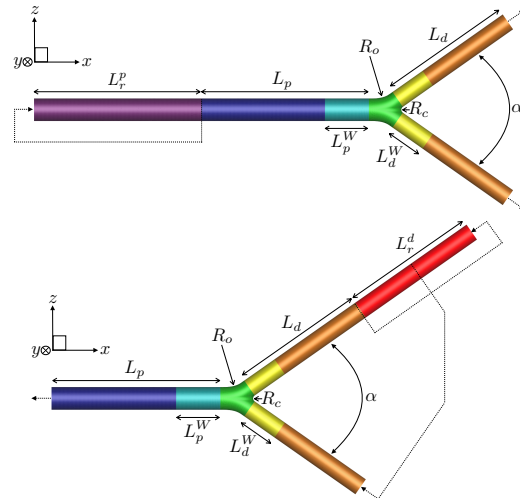

Figure 1. Computational geometries for steady inspiration (top) and steady expiration (bottom). Recycled-inlet and convective-outlet boundary conditions are illustrated with dotted arrows. Only the DNS geometries are shown. For LES, the lengths L_p and L_d of the parent and daughter branches are twice larger. In the RANS geometries, the recycling segments are discarded, while the rest of the inlet sections are reduced to 2/3 of the respective DNS lengths.

GEOMETRY AND COMPUTATIONAL DETAILS

We consider fully developed turbulent flow in a single human airway bifurcation. Distinct geometries are used to simulate steady prolonged inspiration and expiration conditions (see Figure 1). The construction of the geometries is based on the Physiologically Realistic Bifurcation (PRB) model of Heistracher & Hofmann (1995) with the exception of the carinal ridge region. For this region, the PRB model exhibits an unphysical sharp transition between the two mid-plane sides ($y > 0$ and $y < 0$) of the bifurcation. We have refined the construction method to obtain a smooth carina region. The exact mathematical description of our smooth carina will follow in a separate paper. The specific geometric parameters for the single symmetric bifurcation model used in our simulations correspond to the airway generations G3-G4 (see Table 1) in the model of Weibel (1965), where turbulence can still be expected to occur.

To achieve fully developed turbulent inlet profiles we use the recycling boundary conditions at the corresponding entries of the flow (see Figure 1). A recycling length $L_r^p = 15R_p$ is used for the inspiration and $L_r^d = 15R_d$ for the expiration, as recommended by Wu & Moin (2008) for fully developed turbulent flows in straight pipes. The lengths of the parent and daughter branches (L_p and L_d) are extended from the original values given by Weibel (L_p^W and L_d^W) for two reasons: (1) to ensure that the recycling region is not affected by pressure effects upstream of the point where the three pipes merge, and (2) to ensure that the merging region of the three pipes is not affected by outlet effects.

In our simulations we have set the fluid density to $\rho_f = 1$ and the fluid viscosity to $\nu_f = \frac{2}{5300}R_d u_b^d$. Our simulation results are automatically non-dimensionalized by the daughter scales, since we have set the daughter radius to $R_d = 1$ and have ensured that the bulk velocity at each daughter branch is $u_b^d = 1$. Conservation of mass leads to the bulk velocity $u_b^p = 1.29145 u_b^d$ at the parent branch. The recycling inlet conditions ensure that at all times the recycled velocities produce the aforementioned bulk velocity values. The Reynolds number at the parent branch
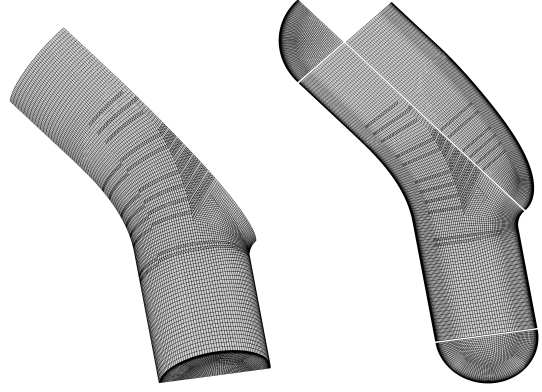

Figure 2. Part of the LES mesh at merging region; Folded (left) and Unfolded (right) mesh. The DNS mesh is almost twice denser in the wall normal direction and exactly twice denser in the other directions. The RANS mesh has the same density with the LES mesh.

is $Re_b^p = \frac{u_b^p D_p}{\nu} = 8517.86$ and at the daughter branches $Re_b^d = \frac{u_b^d D_d}{\nu} = 5300$. The lowest fully turbulent Reynolds number in a pipe flow is known to be around 5300; we have adopted this Reynolds number for the daughter branches to ensure that in all cases the flow is fully turbulent, thus avoiding transitional effects that would be present at lower Re_b^d.

Much attention was given on the mesh generation. As noted by Longest & Vinchurkar (2007), generating structured meshes based on hexahedral elements requires significant time and effort; however these type of meshes are often associated with high quality velocity fields. Unstructured meshes that employ tetrahedral elements can be constructed much faster, but may suffer from increased levels of numerical diffusion, especially in tubular flow systems with a primary flow direction. The results of Vinchurkar & Longest (2008) emphasize the importance of aligning control volume grid lines with the predominant flow direction. They have concluded that multiblock structured and unstructured hexahedral grids have the lowest numerical errors. For this

Table 1. Geometric parameters of the DNS bifurcation geometries. Based on Weibel's model the physical size of daughter radius is $R_d^W = 2.25mm$. In our simulations the geometries are scaled so that the daughter branches have unit radius $R_d = 1.0$.

Parameters	Inspiration / Expiration
Daughter diameter	$D_d = 2\,R_d$
Parent diameter	$D_p = 2\,R_p = 2.48888\,R_d$
Daughter length	$L_d = 15\,R_d$
Parent length	$L_p = 15\,R_p$
Weibel's Daughter length	$L_d^W = 4.08888\,R_d$
Weibel's Parent length	$L_p^W = 3.92857\,R_p$
Recycle lengths	$L_r^p = 15\,R_p\ /\ L_r^d = 15\,R_d$
Outer radius	$R_o = 5.0\,R_d$
Carinal radius	$R_c = 0.4\,R_d$
Split angle	$\alpha = 70°$

Table 2. Details of the parent and daughter pipe regions. The star superscript indicates regional values. The value of the turbulent Reynolds number, Re_τ, is the equivalent for a straight pipe flow at the corresponding bulk Reynolds number, Re_b. The plus superscript indicates normalization with the regional viscous length unit, $\delta_v^* \equiv \nu/u_\tau^*$.

Parameters	Parent LES / DNS	Daughter LES / DNS
$Re_b \equiv \frac{u_b^* D^*}{\nu}$	8517.86	5300
$Re_\tau \equiv \frac{u_\tau^* R^*}{\nu}$	~ 272	~ 181
N_ϕ	200 / 400	136 / 272
N_r	50 / 96	42 / 80
N_s every R^*	18 / 36	12 / 24
$\Delta r_{min}^+ \equiv \frac{Re_\tau^* \Delta r_{min}}{R^*}$	0.5 / 0.333	0.5 / 0.333
$\Delta r_{max}^+ \equiv \frac{Re_\tau^* \Delta r_{max}}{R^*}$	13.0 / 6.4	12.0 / 5.6

reason, we have employed a multiblock unstructured hexahedral mesh (see Figure 2) with prismatic grid patches at the merging region of the pipes to increase the density of the mesh as we move from the low to the high Reynolds number region. In the straight pipe sections, mesh points located at the same radial distance are constructed to have similar control volumes to avoid uneven results; this is particularly important in the case of the Dynamic Smagorinsky LES model, which depends on the local control volumes. The total number of control volumes for the LES simulations is 9.56/8.42 million for the inspiration/expiration geometry, while for the DNS simulations this number reaches 46.0/37.2 million respectively. For the RANS simulations the y and z mirror symmetries permit the reduction of the computational geometries to one quarter and this reduces the number of control volumes to 0.918/0.890 million. It is quite complicated to describe the number of points used in the merging region. One can estimate the mesh density in this region by taking into account Figure 2 and the mesh densities at the straight pipe sections given in Table 2.

EULERIAN FLUID FLOW

In this section, we compare the results from our DNS, LES, and RANS simulations. For both DNS and LES we have used the same constant fluid time step with value $dt_f = 0.004 R_d/U_b^d$. The CFL values produced by this time step rarely exceed 1.1 for the DNS and 0.6 for the LES; note that momentum equations are solved semi-implicitly. Instantaneous results from a pre-calculated turbulent pipe flow at $Re_b^d = 5300$ have been used in both daughter branches for the initialization of the LES expiration flow. Instantaneous results in the fully developed state of the LES expiration flow, manipulated to reverse the flow direction, have been used for the initialization of the LES inspiration flow. Instantaneous results from the LES in the fully developed states have been employed as initial velocity fields for the DNS. Once the inspiration and expiration flows reached their fully developed states, the DNS/LES were continued for 250000/255000 time steps with collection of statistics every 40/1 time steps/step. At the end of the simulations, the statistics were enhanced based on the y and z mirror symmetries of the geometry. For the DNS, no subgrid scale model has been used, while for the LES the Dynamic Smagorinsky model has been adopted. For the RANS simulations the $\overline{v^2} - f$ model has been employed. For the initialization of the RANS simulations we have used the averaged velocity fields from the DNS. The modeled mean flow was solved until the steady state was reached in both inspiration and expiration RANS simulations.

Figure 3 compares the averaged velocity field from the DNS, LES, and $\overline{v^2} - f$ simulations under steady inspiration and expiration conditions. It is evident that the LES results are in excellent agreement with the DNS results. The shape of the in-plane averaged velocity streamlines are almost identical. For the inspiration condition two symmetric, counter rotating, axially oriented secondary vortices are formed at each daughter branch, while for the expiration condition four secondary vortices are formed at the parent branch; note that for each of the aforementioned vortex-systems only one vortex is captured in the cross-sections shown. These secondary vortices (refer to as "Dean vortices") are present even in the laminar regime, their formation being due to centrifugal effects. Dean secondary vortices are formed whenever a straight geometry starts to

curve (for flow in a curved pipe see Dean (1927, 1928)). As the flow moves away from the pipe merging region, curvature effects will no longer contribute to the secondary motion and will eventually dissipate. For the inspiration case a stagnation point is formed at the head of carina. This forces the incoming flow from the parent branch to split into the two daughter branches. The maximum averaged velocity is deflected away from the center and towards the inner walls of the daughter branches. In the outer walls of the daughter branches the averaged velocity is very small, while at the same time there is a short region with backflow (see also the 3D streamlines in Figure 5). The backflow region is formed just after the incoming flow from the parent branch separates from the outer wall of the daughter branches. For the expiration case a high pressure point is formed in front of the carina head. This forces the incoming flow that is traveling close to the inner walls of the daughter branches
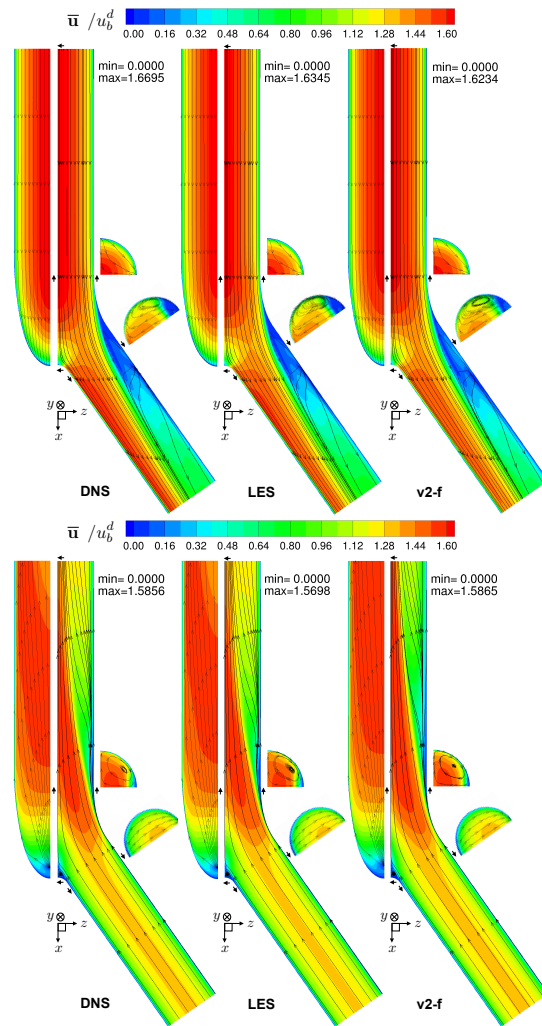

Figure 3. Four different slices of a small part (slightly greater than Weibel's regime) of one quarter of the inspiration and expiration geometries. Contour plots of the averaged velocity magnitude from DNS, LES, and $\overline{v^2} - f$ simulations under steady inspiration (top) and expiration (bottom) conditions. The minimum and maximum values of the contour field are given. The streamlines are constructed from the in-plane averaged velocities of each slice.

3

to form two small vortices at the head of carina; note that only one is shown (see also the 3D streamlines in Figure 5). The rest of the incoming flow from the daughter branches merges at the center of the parent branch. It is evident that the secondary flow field in the bifurcation domain is a result of the bifurcation curvature (i.e. Dean flow effect) and the effect of the carinal ridge shape.

The agreement of the $\overline{v^2} - f$ predictions with the DNS results is striking. As explained, most of the secondary flow features are due to curvature effects and thus the aforementioned agreement is not indicative of the modeling quality of the Reynolds stresses. In fact, when the Reynolds stress components from the DNS are compared to the RANS predictions, many differences are observed. For example, at the inlet pipe sections only the shear stress component is almost identical, while the other components are off. In the straight inlet sections, only the shear stress component is needed to capture the mean flow, and this is why $\overline{v^2} - f$ performs remarkably well at the inlet sections.

Turbulent vortical structures are identified using the Q-criterion (for the definition see Dubief & Delcayre (2000)). Figure 4 illustrates coherent vortical motions formed under steady inspiration and steady expiration conditions. In general, the cores of the vortical structures are parallel to the direction of the local fluctuating vorticity vector. The x component of the normalized fluctuating vorticity vector field is used to color the vortical structures, in order to identify their sense of rotation. Furthermore, the coherent vortical iso-surfaces shown are based on a Q-value that has been chosen so as to highlight the structures at the carina and in the outlet sections. A different Q-value would need to be chosen in order to provide the best possible visualization of the structures in the straight inlet sections. Still, the visualization reveals the existence of quasi-streamwise vortices, similar to the ones observed in straight pipes.
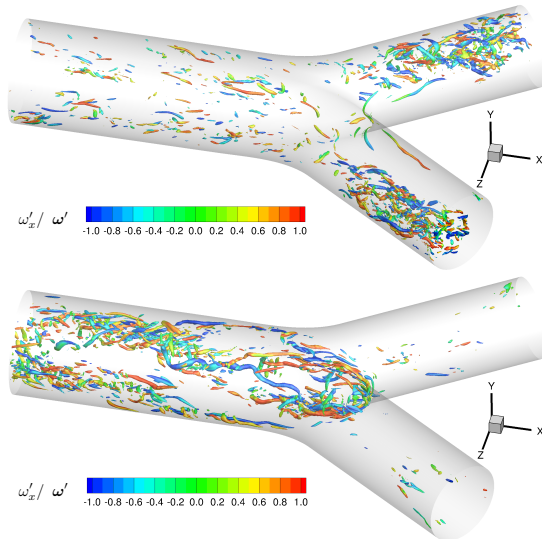

Figure 4.   Turbulent vortical structures identified based on the Q-criterion (utilizing only the fluctuating velocity components) under steady inspiration (top) and expiration (bottom) conditions. Only the Weibel's regime is shown. Iso-surfaces of one positive Q-value at a random instance colored by the x component of the normalized fluctuating vorticity vector field.

During steady inspiration, two counter rotating structures are formed at the carina, one at $y > 0$ and the other at $y < 0$. The two structures follow the contour of the carina region, extending all the way from from one daughter branch and into the other. Just further downstream, two elongated structures are present, one in each daughter branch. As indicated by their color, the vorticity vector associated with the elongated structure in the $z > 0$ branch is parallel to the direction of the mean flow. On the other hand, the vorticity vector of the correspoding structure in the $z < 0$ branch is antiparallel to the mean flow direction. It is quite possible that these structures initially formed at the carina as a single vortex that was subsequently torn apart in the middle due to a locally high shear rate. As the two parts were convected downstream, they were further stretched by the local high speed mean flow to form the aforementioned elongated structures in the inner wall of the daughter branches. In the outer region of the daughter branches, and just after the point where the mean backflow starts, there is a high concentration of structures. These structures do not seem to have a preferential direction of alignment.

During steady expiration, the entire carina becomes a structure generation region. In general, the structures are formed in counter-rotating pairs. Two types of structures are being shed from the head of the carina; structures with extent in the x direction and structures with extent in the y direction (analogous to the mode A and mode B instabilities shed behind a cylinder). There are also fragmented structures extending from the head of carina towards the top and bottom walls of carina. These structures start to elongate once they reach the top and bottom walls of carina. The most interesting structures are formed in the region downstream of the carina and close to the center of the parent branch. These structures have a very large extent, in the order of the parent branch diameter, and have a corkscrew shape. Further downstream and close to the top and bottom walls of the parent branch ($|y| > |z|$), there is a region of very low concentration of structures, while a high concentration of structures (mainly oriented downstream) is found close to the side walls of the parent branch ($|z| > |y|$).

LAGRANGIAN PARTICLE DISPERSION

In the upper bronchial airways, carinal ridges of airway bifurcations are primary hot spots for deposition of inhaled particles. Particle laden flow under laminar conditions has been studied in airway bifurcations, but under turbulent conditions it has never been considered. In this section we examine for the first time the spatial deposition patterns in a bifurcation under full developed turbulent prolonged inspiration and expiration conditions.

The unsteadiness of turbulent conditions demands the time advancement of flow and particle motions to be carried at the same time. Particulate suspensions inhaled by humans are typically dilute and hence the effect of dispersed particles on the carrier fluid, as well as the interactions between particles, can be ignored. To capture all small and large scale flow features that directly affect the motion of particles, we use our high density mesh to accurately resolve the fluid motion via DNS. The dispersed phase is simulated by a Lagrangian approach where particles are continuously released and tracked throughout the domain. The motion of each particle is governed by Newton's second law. In general, particles may experience a set of forces including drag, gravity, buoyancy, lift, electrostatic and many

other. As a first approximation, in our simulations we have considered only the drag force.

The walls of the human airways are covered by a thin layer of colloidal mucous that entraps particles that come into contact with it. For this reason, we can approximate the bifurcation walls as sticky. A particle is deposited by the interception mechanism if its center of mass falls within a distance of one particle radius from the wall surface.

The motion of a spherical rigid particle, based solely on the drag force, is governed by the equations

$$\frac{d\mathbf{u}_p}{dt} = -\frac{\mathbf{u}_p - \mathbf{u}_f(\mathbf{x}_p)}{\tau_p/\alpha} \qquad \frac{d\mathbf{x}_p}{dt} = \mathbf{u}_p \qquad (1)$$

where $\mathbf{x}_p$ and $\mathbf{u}_p$ are the position and velocity of the particle, $\mathbf{u}_f(\mathbf{x}_p)$ is the velocity of the carrier fluid at the position of the particle, $\tau_p = d_p^2 \rho_p / 18 \nu_f \rho_f$ is the particle relaxation time (a measure of the response of the particle to the flow irregularities), $\alpha = 1 + 0.15 Re_p^{0.687}$ is the Schiller & Naumann correction factor introduced to extend the validity of the Stokes drag coefficient up to $Re_p = 800$. The particle Reynolds number is defined as $Re_p = \frac{|\mathbf{u}_p - \mathbf{u}_f(\mathbf{x}_p)| d_p}{\nu_f}$. The parameters d_p and ρ_p represent the diameter and density of the particle, while ν_f and ρ_f represent the viscosity and density of the carrier fluid.

Non-dimensionalization of the particle equations of motion with u_b^d and R_d leads to the formation of the Stokes number $St = \tau_p / \tau_f$, where $\tau_f = R_d / u_b^d$ is the characteristic time scale of the fluid phase. We have simulated particles of five different Stokes numbers with values smaller and larger than unity. The constant particle to fluid density ratio $\rho_p / \rho_f = 750$ has been adopted for all Stokes numbers. This density ratio is in the physical range of particles inhaled by humans. The variability of the Stokes numbers comes from the diameter of the particles. In physical units, the diameters of the particles used in our simulations are in the order of a few μm. If scaled by the daughter branch radius, the diameters of the particles are three orders of magnitude smaller than R_d. Table 3 summarizes the properties of the five different species of particles released and tracked in the bifurcation geometries.

For each one of the five particle species considered, 20 particles were being released at every fluid time step.

Table 3. Particle species (defer in diameter d_p) released and tracked in the bifurcation geometries. The respective Stokes numbers, St, span a range of smaller and larger values than unity. If our geometries are scaled based on the physical size of the airway generations G3-G4 (in the model of Weibel where $R_d^W = 2.25\,\text{mm}$), the physical size of the particles, d_p^W, is in the range of μm.

Species	$d_p^W\,[\mu m]$	$d_p[\times 10^{-3}\,R_d]$	$St = \frac{1}{9}\frac{\rho_p}{\rho_f}\frac{d_p^2}{D_d^2}Re_b^d$
Species 1	2.0	0.88888	0.08724
Species 2	4.0	1.77777	0.34897
Species 3	6.0	2.66666	0.78519
Species 4	8.0	3.55555	1.39588
Species 5	10.0	4.44444	2.18107

The releasing and tracking processes lasted for 25000 fluid time steps. During steady inspiration, the particles were released uniformly and randomly at a cross section normal to the flow direction located at the starting point of the parent pipe branch as defined in Weibel's model. Similarly, for the expiration condition the particles were released at the starting points of the daughter pipe branches as defined in Weibel's model; 10 particles were released from each daughter branch every time step. All five particle cases got the same random initial positions and were injected and tracked at the same time (i.e. they were affected by the same instantaneous flow field). The initial velocity of a particle was chosen to be the same with the instantaneous fluid velocity field at its location of release.

At the end of the simulations (inspiration and expiration) the particles belonging to each of the five species considered were subdivided into three groups: (1) the S^W particles that stuck on the wall of bifurcation that is part of Weibel's regime, (2) the E^W particles that passed through (exited) Weibel's regime, and (3) the A^W particles that are still active in Weibel's regime. The S^W and E^W together form the inactive particles. The total number of particles released for each one of the five species considered and for each simulation (inspiration and expiration) is $T = 500000$ and satisfies the relation $T = S^W + E^W + A^W$. Based on this particle grouping we define the deposition and active fractions. The deposition fraction is defined as the ratio of the deposited particles to the inactive particles $\frac{S^W}{T-A^W}$, while the active fraction is defined as the ratio of the active particles to the total number of particles released $\frac{A^W}{T}$. Table 4 summarizes the values of these fractions for the different particle species and flow conditions considered. It is evident that the deposition fraction increases with increasing particle diameter. On the other hand, the active fraction decreases with increasing particle diameter. Both trends are a direct effect of increasing inertia with increasing particle diameter.

Figure 5 illustrates the correlation between the particle deposition sites and the mean flow vortical structures (along with a number of representative mean flow streamlines). The mean flow structures have: (a) sheet-like shape where the mean flow simply curves, and (b) tube-like shape where the mean flow is of helical motion. The Dean vortices are shown in the respective outlet sections under inspiration and expiration conditions. For the expiration condition, we report for the first time the existence of two vortical structures that follow the shape of the carina; we refer to these structures as the "carinal vortices".

For the inspiration case, the carina region becomes the primary particle deposition site due to direct impaction.

Table 4. Deposition and active fractions for the five particle species during inspiration and expiration.

Species	Inspiration		Expiration	
	$\frac{S^W}{T-A^W}\,[\%]$	$\frac{A^W}{T}\,[\%]$	$\frac{S^W}{T-A^W}\,[\%]$	$\frac{A^W}{T}\,[\%]$
Species 1	0.83	14.20	2.07	15.44
Species 2	20.60	14.79	16.94	13.79
Species 3	53.53	11.09	29.14	12.50
Species 4	75.34	8.70	35.24	11.69
Species 5	87.70	7.45	38.94	10.94

High speed incoming particles reaching the carina cannot turn to follow the local streamlines. Particles released close to the center of the parent pipe have an increased probability to deposit at the head of carina. Due to centrifugal/drifting effects, the areas along the Dean vortices at the daughter branches are the secondary deposition sites for the lighter particles. For the heavier particles, significant deposition takes place even in the straight parent branch. In this section, particles that are close to the wall are affected by the instantaneous sweeps and ejections of the flow. Ejections and sweeps can drive particles away from the wall and towards the wall. Increased deposition at the top and bottom walls of the carina are due to the contraction of geometry which blocks the incoming particles with high inertia. On the other hand, the regions where the side walls of the parent branch meet the diverging external side walls of the daughter branches correspond to particle-free areas. In fact, backflow present in these areas keeps the particles away from the walls. The deposition of heavier particles downstream of the carina, on the inner walls of the daughter branches, is due to a combination of direct impaction and centrifugal/drifting effects.

For the expiration case, particles released closer to the inner walls of the daughter branches have an increased probability to deposit. The carinal vortices drive light and low speed particles towards the wall and thus increase the deposition in this region. Particles deposit also along the Dean vortices due to centrifugal/drifting effects. No deposition occurs on the side walls of the pipe merging region since local velocity tends to drift the particles away form these walls. For the heavier particles, the deposition in the straight daughter sections is the result of instantaneous sweeps and ejections. There is an increased deposition at the top wall, where the daughter branch starts to bend, because the local flow turns before the geometry starts to bend, drifting the particles towards the wall. The deposition at the head of carina reduces for the heavier particles. The enhanced deposition at the top wall (towards $z < 0$ in the parent branch section) is due to the rotational sense of the Dean and carinal vortices that turn particles towards the wall.

SUMMARY AND CONCLUSIONS

We have performed DNS, LES, and RANS simulations in a single human airway bifurcation emulating steady inspiration and expiration conditions. Our simulations show that the predictions of the Dynamic Smagorinsky LES model and the $\overline{v^2} - f$ RANS model are in very good agreement with the DNS results. From our instantaneous DNS flow fields we have identified the regions of increased turbulent vortical activity. From the averaged DNS results we have observed the Dean vortices present also at the laminar level. Here we report for the first time the existence of *carinal vortices* during steady expiration. Using Lagrangian particle tracking we have estaimted the deposition and active fractions for five particle species (deferring in diameter). Preferential deposition sites have been identified and a correlation with the mean flow characteristics has been established. Our results can be used as reference in modeling studies of particle laden flows in airway bifurcations.
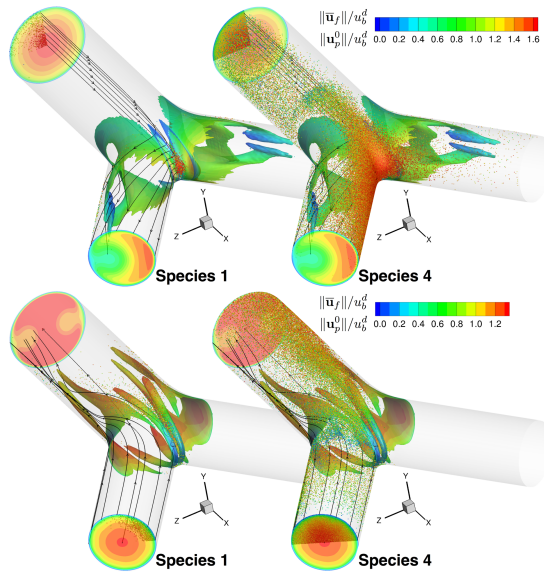

Figure 5. Initial release locations and final deposition locations of particles from Species 1 (left) and Species 4 (right) under steady inspiration (top) and expiration (bottom) conditions. Only the Weibel's regime is shown. The slices, colored with the mean fluid velocity magnitude, represent the inlet and outlet locations of Weibel's geometry. Particles are colored by their initial velocity magnitude (obtained from the instantaneous fluid velocity at the time and location of release). Only the particles that stuck in the Weibel's regime and had initial release location with $y_p^0 \geq 0$ and $z_p^0 \geq 0$ are shown. For these particles their initial and final locations are illustrated. The iso-surfaces of the mean flow vortical structures, identified with the Q-criterion (utilizing only the mean velocity field), are colored with the mean fluid velocity magnitude. Representative streamlines based on the mean velocity vector field are shown.

REFERENCES

Dean, W.R. 1927 Xvi. note on the motion of fluid in a curved pipe. *The London, Edinburgh, and Dublin Philosophical Magazine and Journal of Science* **4** (20), 208–223.

Dean, W.R. 1928 Lxxii. the stream-line motion of fluid in a curved pipe (second paper). *The London, Edinburgh, and Dublin Philosophical Magazine and Journal of Science* **5** (30), 673–695.

Dubief, Y. & Delcayre, F. 2000 On coherent-vortex identification in turbulence. *Journal of turbulence* **1** (1), 011–011.

Heistracher, T. & Hofmann, W. 1995 Physiologically realistic models of bronchial airway bifurcations. *Journal of Aerosol Science* **26** (3), 497–509.

Longest, P. & Vinchurkar, S. 2007 Effects of mesh style and grid convergence on particle deposition in bifurcating airway models with comparisons to experimental data. *Medical Engineering & Physics* **29** (3), 350–366.

Vinchurkar, S. & Longest, P. 2008 Evaluation of hexahedral, prismatic and hybrid mesh styles for simulating respiratory aerosol dynamics. *Computers & Fluids* **37** (3), 317–331.

Weibel, E.R. 1965 *Morphometry of the human lung*. Springer.

Wu, X. & Moin, P. 2008 A direct numerical simulation study on the mean velocity characteristics in turbulent pipe flow. *Journal of Fluid Mechanics* **608**, 81–112.